MEASUREMENTS OF FLOW SPEEDS IN THE CORONA BETWEEN 2 AND 30 $R_\odot$

N. R. SHEELEY, JR., Y.-M. WANG, S. H. HAWLEY,[1] G. E. BRUECKNER, K. P. DERE, R. A. HOWARD,
M. J. KOOMEN,[2] C. M. KORENDYKE, D. J. MICHELS, S. E. PASWATERS,[3] D. G. SOCKER,
O. C. ST. CYR,[4] AND D. WANG[3]

E. O. Hulburt Center for Space Research, Naval Research Laboratory, Washington DC 20375-5352

P. L. LAMY AND A. LLEBARIA
Laboratoire d'Astronomie Spatiale, F-13376 Marseille Cedex 12, France

R. SCHWENN
Max Planck Institut für Aeronomie, D-37189 Katlenburg-Lindau, Germany

AND

G. M. SIMNETT, S. PLUNKETT, AND D. A. BIESECKER
Space Research Group, School of Physics and Space Research, University of Birmingham, Birmingham B15 2TT, England, UK

ABSTRACT

Time-lapse sequences of white-light images, obtained during sunspot minimum conditions in 1996 by the Large Angle Spectrometric Coronagraph on the *Solar and Heliospheric Observatory*, give the impression of a continuous outflow of material in the streamer belt, as if we were observing Thomson scattering from inhomogeneities in the solar wind. Pursuing this idea, we have tracked the birth and outflow of 50–100 of the most prominent moving coronal features and find that:

1. They originate about 3–4 $R_\odot$ from Sun center as radially elongated structures above the cusps of helmet streamers. Their initial sizes are about 1 $R_\odot$ in the radial direction and 0.1 $R_\odot$ in the transverse direction.

2. They move radially outward, maintaining constant angular spans and increasing their lengths in rough accord with their speeds, which typically double from 150 km s^{-1} near 5 $R_\odot$ to 300 km s^{-1} near 25 $R_\odot$.

3. Their individual speed profiles $v(r)$ cluster around a nearly parabolic path characterized by a constant acceleration of about 4 m s^{-2} through most of the 30 $R_\odot$ field of view. This profile is consistent with an isothermal solar wind expansion at a temperature of about 1.1 MK and a sonic point near 5 $R_\odot$.

Based on their relatively small initial sizes, low intensities, radial motions, slow but increasing speeds, and location in the streamer belt, we conclude that these moving features are passively tracing the outflow of the slow solar wind.

Subject headings: solar wind — Sun: corona — Sun: particle emission

1. INTRODUCTION

Measurements of solar wind speed now extend almost everywhere within the heliosphere. In situ measurements have been obtained at low latitudes from 0.3 ($\sim$60 $R_\odot$) to 50 AU and at high latitudes from 2 to 4 AU (Schwenn 1990; Richardson et al. 1995; Phillips et al. 1995). Also, solar wind speeds have been inferred from radio scintillation measurements at all latitudes (Rickett & Coles 1991; Kojima & Kakinuma 1990; Watanabe 1989), and at distances that now reach within 20 $R_\odot$ of the Sun (Coles et al. 1991). The only unexplored region lies closer to the Sun where spacecraft have not yet gone, where the radio scintillation measurements are still scarce, and, perhaps most importantly, where the wind is accelerated. This paper describes the first synoptic observations of this final unexplored region obtained remotely with the Large Angle Spectrometric Coronagraph (LASCO) on the *Solar and Heliospheric Observatory* (*SOHO*) spacecraft (Brueckner et al. 1995).

Time-lapse sequences of white-light coronal images, obtained with the nested coronagraphs C2 (2.2–6 $R_\odot$) and C3 (3.7–30 $R_\odot$) on *SOHO*, show what appears to be a continual outflow of material from the Sun (Brueckner 1996). The streamer-belt location of this flow and its 100–300 km s^{-1} speed suggest that we are observing Thomson scattered emission from inhomogeneities in the slow solar wind as it begins to accelerate from the Sun. The effect is so obvious that one can always tell the direction of time by looking at coronal streamers, the uppermost portions of which seem to be intermittently torn away and carried outward by the flow. The direction of time is not obvious over the polar coronal holes, where there are numerous plumes but no lateral inhomogeneities to trace the flow.

This paper presents our first measurements of this flow field using the moving intensity features as tracers. In effect, we are determining the properties of a steady flow by looking at transient features being carried by it, like "leaves in the wind."

2. THE OBSERVATIONS

The moving coronal features are best seen in sequences of running difference images obtained by subtracting the pre-

---

ceding frame (taken 1 or 2 hr earlier) from the current one. In such images, the moving features are indicated by "bipolar" areas, in which the lighter segment leads in the direction of motion and the darker segment follows. Quantitatively, these "bipoles" are similar to those obtained by subtracting slightly shifted Gaussian profiles: The intensity is jointly proportional to the amount of shift and the slope of the intensity profile. Also, the light-dark separation indicates the spatial size of the shifted feature and is independent of the amount of shift, provided that the shift is not large enough to separate the profiles completely.

Figure 1 (Plate 13) shows a sequence of running difference images during the birth and outward motion of a moving coronal feature on 1996 May 24. The enhancement is first seen in the C2 image at 0651 UT as an elongated "bipolar" feature greatly stretched in the radial direction with its black trailing segment just above the cusp of a helmet streamer at 3.6 $R_\odot$. Its "pole separation" was about 1.3 $R_\odot$ at that time, but increased to about 4.0 $R_\odot$ by 1418 UT when the feature had moved to 12.2 $R_\odot$ and was observed with the C3 coronagraph. Thus, although we refer to these features as small, they are initially almost as large as the Sun itself and they double or triple their size as they move out through the 30 $R_\odot$ field of view of the coronagraph.

After 1418 UT, the leading intensity started to fade relative to the trailing intensity, so that the black-white separation no longer provided an accurate indication of the radial size of the feature. This invariably happens in the outer part of the C3 field of view, indicating that the intensity profile weakens significantly during the 1 or 2 hr time shift between frames.

As one can appreciate from Figure 1, it is easier to trace the outward progress of these moving coronal features than it is to determine the details of their origin. When we track them backward in time, we eventually lose them in the array of linear structures extending from the tops of helmet streamers. We have never seen them in accompanying observations of the lower corona obtained with the C1 coronagraph (with a field of view extending from 1.1 to 2.8 $R_\odot$). Thus, although the details of their origin are not yet clear, these features seem to be born high in the corona above the tops of helmet streamers and not near the surface of the Sun.

Figure 2 (Plate 14) shows the origin of another moving coronal feature on 1996 October 30. The sequence begins at 0755 UT with the enhancement of a helmet structure. By 0840 UT, the enhancement extends nearly continuously to 3.7 $R_\odot$, where two bright spikes are visible above the tops of adjacent helmets. However, by 0925 UT, the connection is no longer continuous; the bright features have moved out to 5.8 $R_\odot$, and dark depleted regions are clearly visible behind them. From this time onward, these features have the characteristic "bipolar" appearance of isolated moving density enhancements.

At this point, it is natural to wonder whether these moving coronal features might be very small coronal mass ejections (CMEs). Their elongated shapes and their movement along helmet streamers are consistent with the "jet along a streamer" category of CME that Howard et al. (1985) identified in the SOLWIND coronagraph observations. As we shall see below, the relatively low intensities and slow speeds of these features are also consistent with this identification. On the other hand, we shall also find that their radial speed profiles $v(r)$ tend to cluster around a common path, indicating a more passive control by the solar wind than one finds for the wider variety of CMEs.

To obtain an idea of how strong these enhancements are, we measured the intensity of a bright feature on a C2 difference image at 2343 UT on 1996 May 26 and compared it with the unsubtracted K-coronal intensity of the streamer a few hours earlier. We used an image of polarized brightness to separate the K corona from the F corona, assumed to be largely unpolarized. The polarized intensity was derived from images obtained through three separate Polaroids oriented 60° apart, in the manner described by Gibson (1973) and Brueckner et al. (1995). The intensity of the bright feature was 7% ± 2% of the background K-coronal intensity, suggesting that the moving coronal features are probably more like passive tracers of the solar wind mass flow than major contributors to it.

Figures 3 and 4 show tracking measurements for the moving density features in Figures 1 and 2. The height/time measurements (*top panels*) are repeatable with an accuracy comparable to or slightly larger than the 0.5 $R_\odot$ size of the symbols used to plot them. In each case, the solid curve is the root mean square best fit to the equally weighted points using a second-order polynomial of the form

$$r = r_0 + v_0 t + \tfrac{1}{2}at^2 \ . \qquad (1)$$

The parameters r_0 and v_0 are the position and speed at the time of the first measurement, and a is the constant acceleration associated with the quadratic fit. The corresponding speed/height relation is

$$v^2 = 2a(r - r_1) \ , \qquad (2)$$

where r_1 is the radius that the speed vanishes and is related to the fit parameters by $r_1 = r_0 - v_0^2/(2a)$. However, it does not make sense to extrapolate the profile back to $r = r_1$ because the feature did not exist prior to the time $t = 0$, when we first measured it. Thus, the speed v does not vanish unless v_0 itself happens to vanish.

Each position measurement was obtained at the midpoint of the "neutral line" between the leading (white) and trailing (black) area on the running difference image. Consequently, the measured height does not refer to the centroid of the moving feature at the end time of the difference interval (when it was plotted), but to a position intermediate between the starting and ending times of that interval. This means that the measured heights depend slightly on the separation used for the difference images as well as on the evolution of the intensity profile of the moving feature (which weakens toward the outer region of the C3 field of view). We have not yet corrected for these effects.

On the other hand, the position angles should be relatively insensitive to these effects, especially when these angles do not change with time. This is the case for the May 24 and October 30 events, the position angles of which remained essentially constant at 100°.2 and 91°.5 through the course of these measurements (*middle panels*).

We have tried two methods of obtaining the speed profile $v(r)$ from the height/time measurements. One method is to derive the speed profile from the smooth fit to the height/time points using equation (2). This method has the advantage of removing a variety of measurement errors including slight mismatches between the C2 and C3 fields of view. However, a disadvantage is that the resulting speed profile may be locally inaccurate, especially toward the beginning and end of the profile. Another method is to determine the
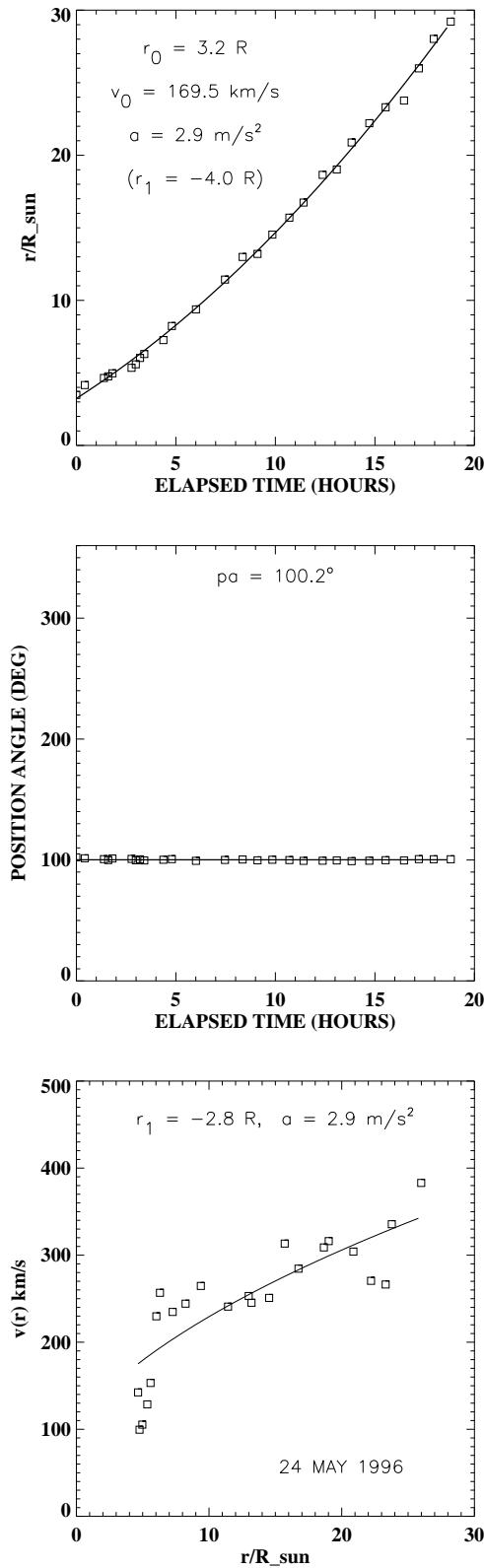
FIG. 3.—Tracking measurements for the 1996 May 24 moving coronal feature shown in Fig. 1. In the top panel, the smooth curve is the best fit to the equally weighted measurements using a second-order polynomial of the form given by eq. (1). In the middle panel, the solid line is the average of the individual measurements. In the bottom panel, the speed measurements are five-point running straight-line fits to the height/time measurements in the top panel, and the solid line is the best fit to these points using the function given by eq. (2).
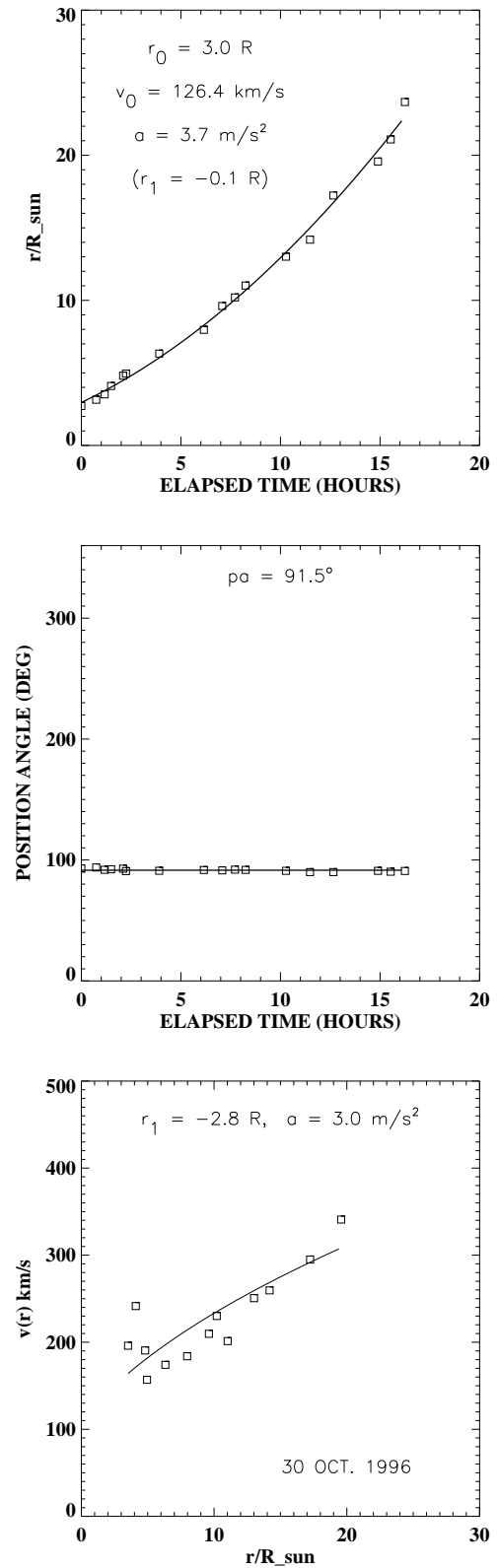
FIG. 4.—Same as Fig. 3, but for the 1996 October 30 event shown in Fig. 2.

speed directly from the height/time data points by means of a running straight-line fit. This procedure does not depend on the global fit to all of the points, but it amplifies the local measurement errors, giving a large scatter to the points that must then be fit by a speed profile. Hopefully, one would be

able to reduce this scatter by combining measurements for a large number of events.

We used the latter method to derive the speed measurements in the lower panels of Figures 3 and 4. A five-point running straight-line fit to the height/time measurements was used in this determination. As one can see, the small positional errors in the upper panels have been amplified considerably, giving a large scatter to the points in the lower panels. The solid curves represent the best fit to these points, which again are given equal weight, using equation (2). As one can see, the resulting accelerations are comparable to those obtained from the global fits to the height/time measurements (cf. upper and lower panels) and lie in the range 2.9–3.7 m s^{-2}.

Some events show much less scatter. This was true for the 1996 April 30 event, the measurements of which are shown in Figure 5. Like the previous two examples, this one also moved radially outward, as indicated in the middle panel. The quadratic fit to the height/time measurements gives an acceleration of 5.3 m s^{-2}. The speed measurements in the lower panel were obtained using the five-point running straight-line fit method and are independent of the global fit used in the upper panel. Thus, we may use a different profile to fit them. Here, we have used a function of the form

$$v^2 = v_a^2 [1 - e^{-(r-r_1)/r_a}] , \qquad (3)$$

which retains the parabolic shape of equation (2) when $r \approx r_1$, but bends more sharply to approach an asymptotic speed v_a when $r - r_1 \gg r_a$. In effect, both equations (2) and (3) give the kinetic energy per particle as a function of r, but the former continues linearly while the latter levels off.

As indicated in the bottom panel of Figure 5, equation (3) provides a good fit to the speed/height measurements when $r_1 = 4.5 \, R_\odot$, $r_a = 15.2 \, R_\odot$, and $v_a = 418.7$ km s^{-1}. We have also fit these speed/height points with a quadratic function of the form given by equation (2) and obtained $r_1 = 3.7 \, R_\odot$ and $a = 5.0$ m s^{-2}, the values of which are reassuringly close to those obtained directly from the height/time plot in the upper panel. However, the constant acceleration does not fit the measured points as well as the exponential relation, which has a shape initially steeper and ultimately flatter than that of the parabola (not shown here).

Figure 6 summarizes our measurements for about 65 individual moving features. The speeds in the top panel were obtained by applying the five-point running linear fit to the height/time measurements, whereas the speeds in the middle panel were obtained from the direct fits to the height/time curves. In each case, the points are better organized along an outward path than are those from CMEs shown in the bottom panel for comparison. The speeds of these CMEs range widely from 100 km s^{-1} to 700 km s^{-1}, as if they had independent sources of acceleration. By contrast, the quasi-parabolic profile of the radially moving features suggests that they are carried passively by the solar wind.

In the upper and middle panels, the magnitude of the scatter is ~ 150 km s^{-1} which is comparable to the range of *in situ* speeds found in the slow solar wind at Earth. Thus, although some of the scatter may be due to projection effects, an appreciable part may be due to intrinsic variations of wind speed near the Sun.

An interesting characteristic of this scatterplot is the "corner" near (7 $R_\odot$, 225 km s^{-1}) in the upper panel. We do not yet know the origin of this feature. It may be an
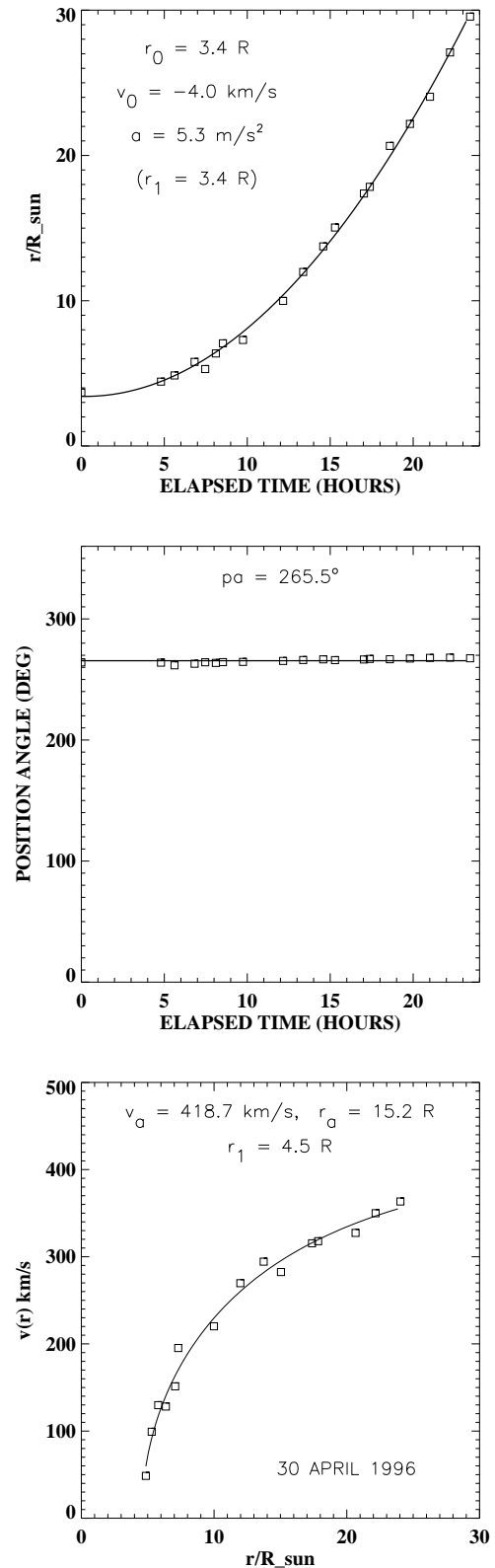

FIG. 5.—Same as Fig. 3, but for the 1996 April 30 event. The best fit to the speed/height points was obtained using the exponential function given by eq. (3).

artifact of the running-fit method of velocity determination, because it does not occur in the middle panel. On the other hand, it represents the result of combining measurements for 65 independent events and might be a valid indication of
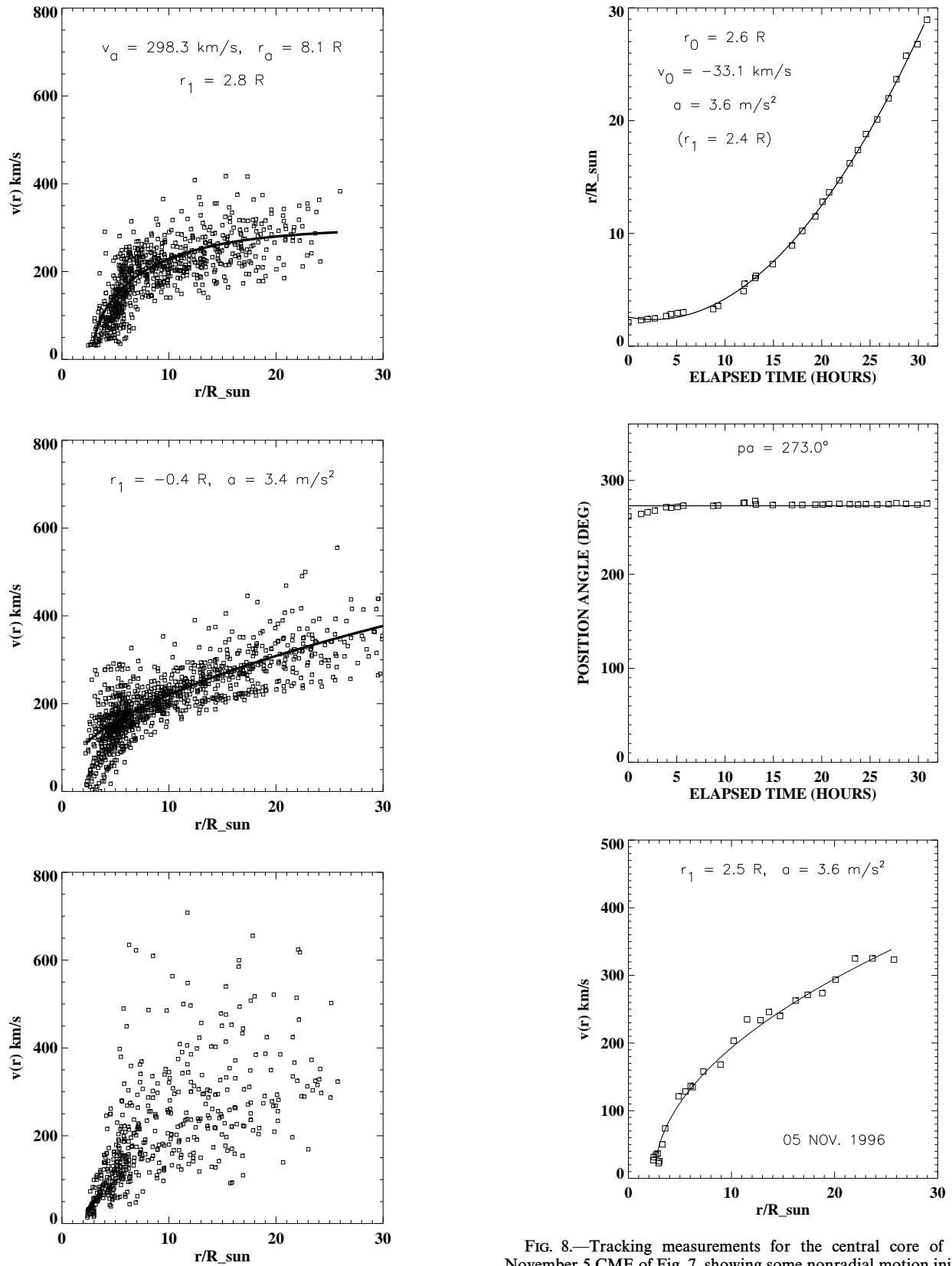
FIG. 6.—Speed/height measurements for 65 individual moving density enhancements (*top and middle panels*) and for 38 CMEs (*bottom*), showing the tendency of the moving density enhancements to cluster along a quasi-parabolic path. In the top panel, the measurements were derived using the running straight-line fit method, while those in the middle panel were obtained from the global fits to the height/time measurements. The solid curves in the top and middle panels are best fits to the unweighted data points, using eqs. (3) and (2), respectively.

FIG. 8.—Tracking measurements for the central core of the 1996 November 5 CME of Fig. 7, showing some nonradial motion initially and a parabolic speed profile similar to those of Figs. 3–6.

a more rapid change in the speed profile than is obtained from the simple parabola. For this reason, we chose to fit those points with the exponential profile given by equation (3). This function provides the steep initial rise and sub-

sequent leveling off that these data points require. And, of course, it has an extra fit parameter.

The points in the middle panel of Figure 6 reflect the smooth behavior of the quadratic fits to the height/time profiles. Although this panel does not show the "corner" near (7 $R_\odot$, 225 km s^{-1}), it shows a cloud of points near (5 $R_\odot$, 150 km s^{-1}) where many profiles seem to begin. The solid curve represents the best fit to these points using the quadratic profile given by equation (2), again weighting the points equally. The resulting acceleration of 3.4 m s^{-2} is comparable to the values obtained in Figures 3–5. Although the solid curve provides a plausible fit to most of the points, including the cloud near (5 $R_\odot$, 150 km s^{-1}), it does not bend sharply enough to match the ones that begin with very low speed.

In general, CMEs tend to have their own dynamic speed profiles. However, some CME-related features seem to move passively outward with speed profiles similar to those in Figures 3–6. The central core of the 1996 November 5 CME in Figure 7 (Plate 15) is such a passive feature. It is an eruptive prominence, with an origin near the Sun that was seen in Hα by the C1 coronagraph. The expanding cavity and central core are clearly visible coming out from under the C2 occulting disk at 0725 UT, and the central core is still visible at 0910 UT when it was 18 $R_\odot$ from Sun center. The streamer itself disappeared for 1 or 2 days following the event, suggesting that this was a "streamer blowout" CME as defined by Howard et al. (1985). Unlike other CMEs, "streamer blowouts" maintain their occurrence rate during sunspot minimum when they are the most commonly occurring type of mass ejection (Howard et al. 1986).

Figure 8 shows tracking measurements for the central core of this 1996 November 5 CME as it moved through the C2 and C3 fields of view. Both the height/time points and the speed/height points are well fit by quadratic curves with an acceleration $a = 3.6$ m s^{-2}, which is comparable to the values obtained in Figures 3–6. Also, these quadratic fits give starting radii $r_1 \approx 2.5$ $R_\odot$, which is essentially where the central core was first seen as it emerged from beneath the occulting disk at 2.2 $R_\odot$. Thus, the initial speed of this eruptive prominence was much lower than the starting speeds of most of the moving coronal density enhancements. Another difference is that the eruptive prominence had some nonradial motion, drifting northward by 15° while it was moving from 2 $R_\odot$ to 3 $R_\odot$, whereas the coronal density enhancements move radially.

3. SUMMARY AND DISCUSSION

The measurements described above are preliminary and do not include corrections for possible sources of error such as the matching of C2 and C3 measurements, the identification of the centers of the respective fields of view, and the effect of using "neutral lines" to track features on difference images. Also, there has been no allowance for the possibility that some of the moving features were out of the sky plane and that their measured speeds were underestimates. All of these effects will be considered in the future.

However, it seems doubtful that such future considerations will change the overall trend of the measurements. We have seen that small density enhancements originate above the cusps of helmet streamers and move radially outward with a nearly constant acceleration. Their speed scatterplots cluster closely around a parabolic shape with an acceleration of about 3.5 m s^{-2}. This is in marked

contrast to similar scatterplots for CMEs, the speeds of which vary widely from event to event. Apparently, we are observing bits of helmet streamers being torn away by the slow solar wind and carried passively outward as tracers of the wind speed.

Such an observed speed profile can be used as an empirical constraint on the classic solar wind equations. Traditionally, the problem of a radial flow has been solved by combining the equations of momentum and mass flow with an assumed energy relation (Parker 1963; Holzer 1988 and references contained therein). Now, we can obtain closure by replacing the poorly known energy relation with the empirically determined speed profile. This will enable us to derive the temperature (and thus sound speed) as a function of radial distance from the Sun and to determine the location of the sonic point.

We begin with the momentum equation for a steady state radial flow

$$\rho v \frac{\partial v}{\partial r} = -\frac{\partial p}{\partial r} - \frac{GM\rho}{r^2} , \qquad (4)$$

where ρ is the ion density, v is the radial flow speed, p is the effective pressure, G is the gravitational constant, and M is the mass of the Sun. Then we add the steady state mass flow equation

$$\rho v r^2 = \text{const} . \qquad (5)$$

This steady state condition breaks down at $r = r_1$ where $v = 0$, and it returns us to the question of how to interpret the observations near the start of the profile. In § 2, we saw some evidence that the motion begins near 5 $R_\odot$ with a finite speed of about 150 km s^{-1}. On the other hand, the initial speed is much smaller for some events, as it was for the moving density enhancement of April 30 and the CME of November 5 (see Figs. 5 and 8). In such cases, there must be an interval of time for the tracers to be brought up to the speed of the wind.

We continue by assuming that the effective coronal temperature T is a function of radial distance and is related to the pressure by the equation

$$p = 2nkT , \qquad (6)$$

where k is the Boltzmann constant, n is the proton density given by $n = \rho/m_p$, and m_p is the mass of the proton. Defining a sound speed v_s by $v_s^2 = \partial p/\partial \rho = 2kT/m_p$, and combining equations (4)–(6), we find

$$\frac{\partial}{\partial r}\left(\frac{v_s^2}{vr^2}\right) = -\left(\frac{1}{vr^2}\right)\left(v\frac{\partial v}{\partial r} + \frac{GM}{r^2}\right), \qquad (7)$$

where v is the empirically determined speed profile given by equation (2) or equation (3).

Now, the right-hand side of equation (7) is a known function of r that can be integrated from the lower limit r to an upper limit $r_{\max}$. The result can be written as:

$$\frac{v_s^2(r)}{v(r)r^2} - \frac{v_s^2(r_{\max})}{v(r_{\max})r_{\max}^2} = \int_r^{r_{\max}}\left(\frac{1}{vr^2}\right)\left(v\frac{\partial v}{\partial r} + \frac{GM}{r^2}\right)dr . \qquad (8)$$

The second term of this equation is an unknown constant of integration. However, it tends to zero as $r_{\max}$ becomes large, and can be neglected relative to the first term for $r \ll r_{\max}$. Ideally, we would let $r_{\max}$ become infinite and drop the second term entirely. However, in our case, this would

mean extrapolating $v(r)$ beyond 30 $R_\odot$. Another approach would be to set $r_{max} = 30\ R_\odot$ and calculate $v_s(r)$ as if the unknown second term were zero. We could then use the calculated value of $v_s(r_{max})$ to evaluate the second term and see whether its neglect was justified. Figure 9 shows the results obtained using both of these methods.

The top panel of Figure 9 shows a parabolic speed profile $v(r)$ obtained from equation (2) with $r_1 = 2.1\ R_\odot$ and $a = 3.6$ m s^{-2}, together with two versions of the derived sound speed profile $v_s(r)$. The solid curve was obtained from equation (8) by setting $r_{max} = 30\ R_\odot$ and neglecting the second term. The dashed curve was obtained by setting
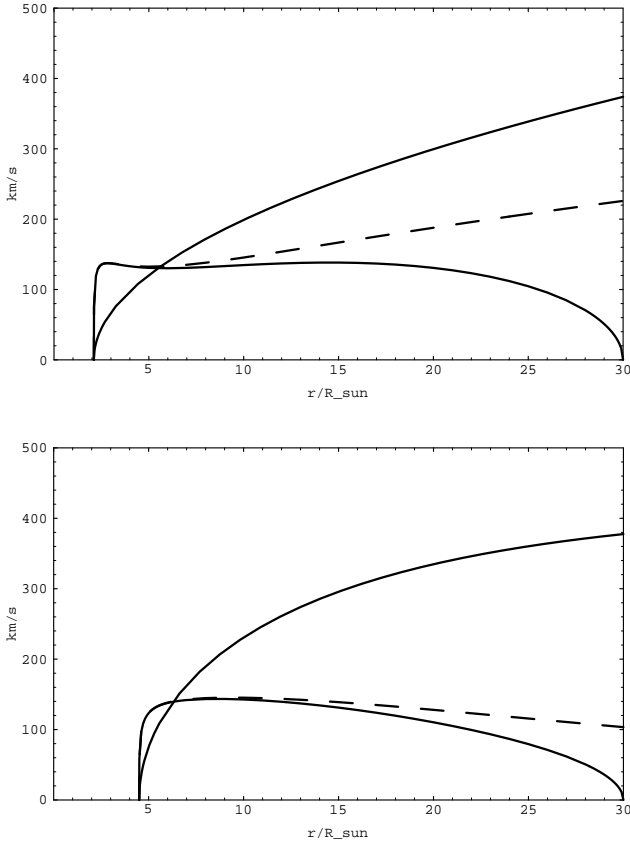
FIG. 9.—*Top:* Wind speed profile obtained from eq. (2) with $a = 3.6$ m s^{-2} and $r_1 = 2.1\ R_\odot$ (*parabolic solid curve*), and the sound speed profile derived in two different ways (*flat solid and dashed curves*). *Bottom:* Same as the top panel, but obtained from eq. (3) with $r_1 = 4.5\ R_\odot$, $v_a = 418.7$ km s^{-1}, and $r_a = 15.2\ R_\odot$. In each case, the sound speed has a plateau at 130–140 km s^{-1}, corresponding to a temperature of about 1.1 MK and a sonic point near 5–6 $R_\odot$.

$r_{max} = \infty$ and using equation (2) to extrapolate the speed profile. The two curves have the same behavior out to about 15 $R_\odot$, when the dashed curve starts to show the effect of the parabolic extrapolation and the solid curve starts to fall toward zero. However, closer to the Sun, these curves are nearly identical, rising suddenly at $r = r_1$ and remaining on a 130 km s^{-1} plateau until they start to separate in the range 10–15 $R_\odot$. As discussed above, the steady state assumption breaks down at the start where $v = 0$, so the sudden rise is spurious. However, the 130 km s^{-1} plateau makes sense, and corresponds to an isothermal expansion at a temperature of 1.0 MK, in nearly perfect agreement with Parker's (1963) original calculation (cf. his Fig. 6.1). Also, the intersection of this plateau with the speed profile $v(r)$ gives a sonic point $r_s = 5.5\ R_\odot$.

The bottom panel of Figure 9 gives a similar result. Here, we show the exponential speed profile $v(r)$ obtained from equation (3) with $r_1 = 4.5\ R_\odot$, $v_a = 418.7$ km s^{-1}, and $r_a = 15.2\ R_\odot$, as deduced from the 1996 April 30 measurements in Figure 5. The two different sound speed profiles $v_s(r)$ are again indicated by the predominantly flat solid and dashed curves, which remain together until well after 15 $R_\odot$. Their common plateau lies at 140 km s^{-1}, corresponding to 1.2 MK. Also, their intersection with the wind speed profile $v(r)$ gives a sonic radius $r_s = 6.5\ R_\odot$. This is close to the value of 5.5 $R_\odot$ obtained in the upper panel despite the much greater starting radius of the 1996 April 30 event.

The essence of these calculations is that they give a nearly isothermal sound speed of 130–140 km s^{-1}, which provides a simple way of estimating the location of the sonic point from the observed speed profiles. For most profiles, the sonic point lies in the vicinity of 5–6 $R_\odot$. Finally, we note that for quadratic speed profiles, the integration can be done analytically to obtain an approximate solution: $v_s \approx 100a^{1/4}$ km s^{-1}, $T \approx 0.6a^{1/2}$ MK, and $r_s \approx r_1 + 7.2a^{-1/2}$ with a in m s^{-2}.

REFERENCES

Brueckner, G. E. 1996, Trans. AGU (EOS), 77, S204
Brueckner, G. E., et al. 1995, Sol. Phys., 162, 357
Coles, W. A., Esser, R., Lovhaug, U.-P., & Markkanen, J. 1991, J. Geophys. Res., 96, 13849
Gibson, E. G. 1973, The Quiet Sun, NASA SP-303 (Washington: GPO) 265
Holzer, T. E. 1988, in Proc. Solar Wind 6, ed. V. J. Pizzo, T. Holzer, & D. G. Sime, NCAR Tech. Note TN-306, 3
Howard, R. A., Sheeley, N. R., Jr., Koomen, M. J., & Michels, D. J. 1985, J. Geophys. Res., 90, 8173
Howard, R. A., Sheeley, N. R., Jr., Michels, D. J., & Koomen, M. J. 1986, in The Sun and the Heliosphere in Three Dimensions, ed. R. G. Marsden (Dordrecht: Reidel), 107

Kojima, M., & Kakinuma, K. 1990, Space Sci. Rev., 53, 173
Parker, E. N. 1963, Interplanetary Dynamical Processes (New York: Wiley)
Phillips, J. L., et al. 1995, Science, 268, 1030
Richardson, J. D., Belcher, J. W., Lazarus, A. J., Paularena, K. I., Gazis, P. R., & Barnes, A. 1995, in Proc. Solar Wind 8, ed. D. Winterhalter, J. T. Gosling, S. R. Habbal, W. S. Kurth, & M. Neugebauer (Woodbury: AIP), 586
Rickett, B. J., & Coles, W. A. 1991, J. Geophys. Res., 96, 1717
Schwenn, R. 1990, Large-Scale Structure of the Interplanetary Medium, in Physics of the Inner Heliosphere Vol. 1, Large-Scale Phenomena (Berlin: Springer), 99
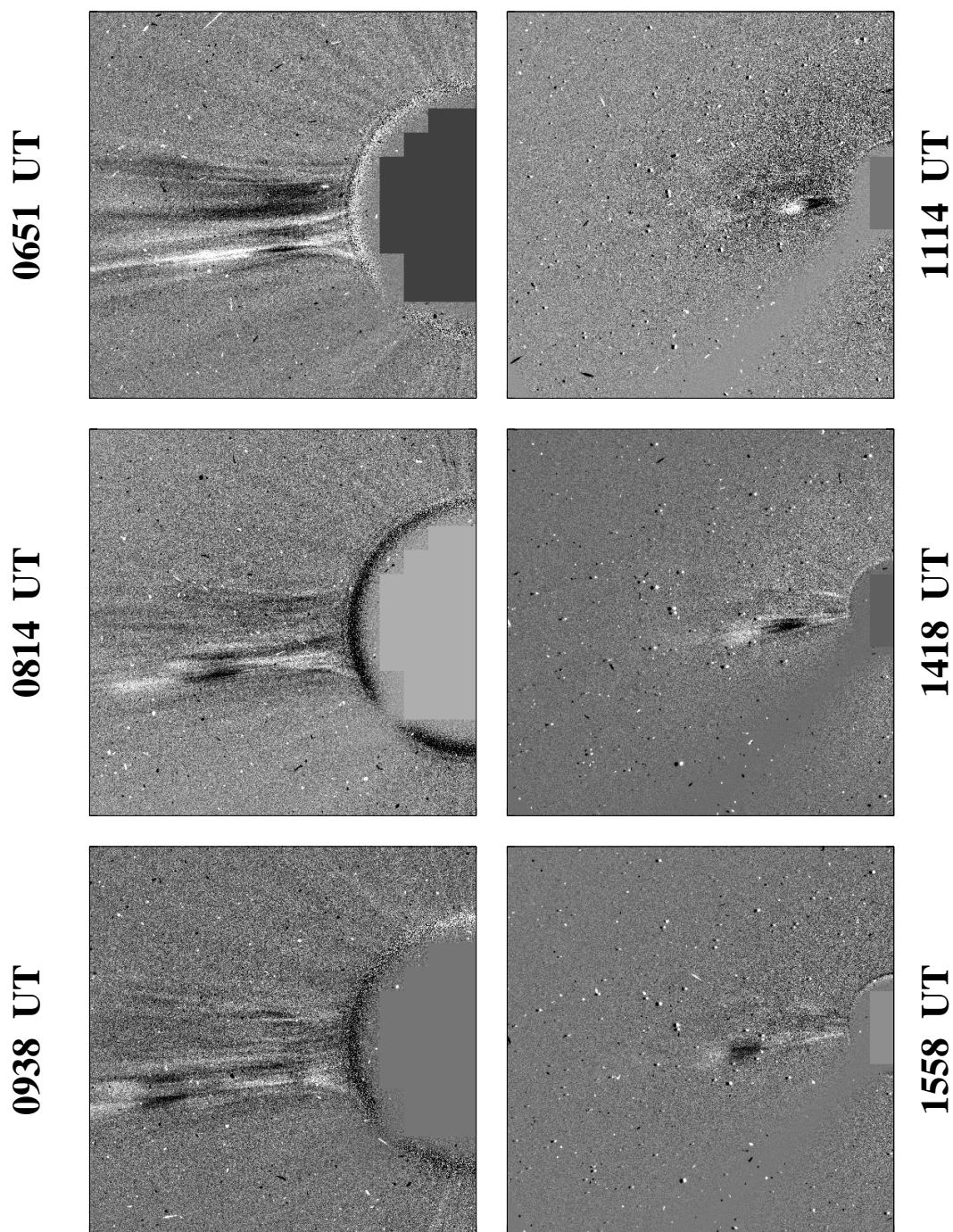Watanabe, T. 1989, Adv. Space Res., 9 (4), 99

FIG. 1.—The formation and outward movement of a coronal density enhancement on 1996 May 24, as seen in running difference images obtained with the C2 (*left*) and C3 (*right*) coronagraphs. The scales are provided by the occulting disks, the radii of which are 2.2 and 3.7 $R_\odot$, respectively. In these difference images, proper motions are indicated by "bipolar" areas with white portions leading in the direction of motion and with black portions following. The very small bipolar features scattered over the C3 field of view are stars.

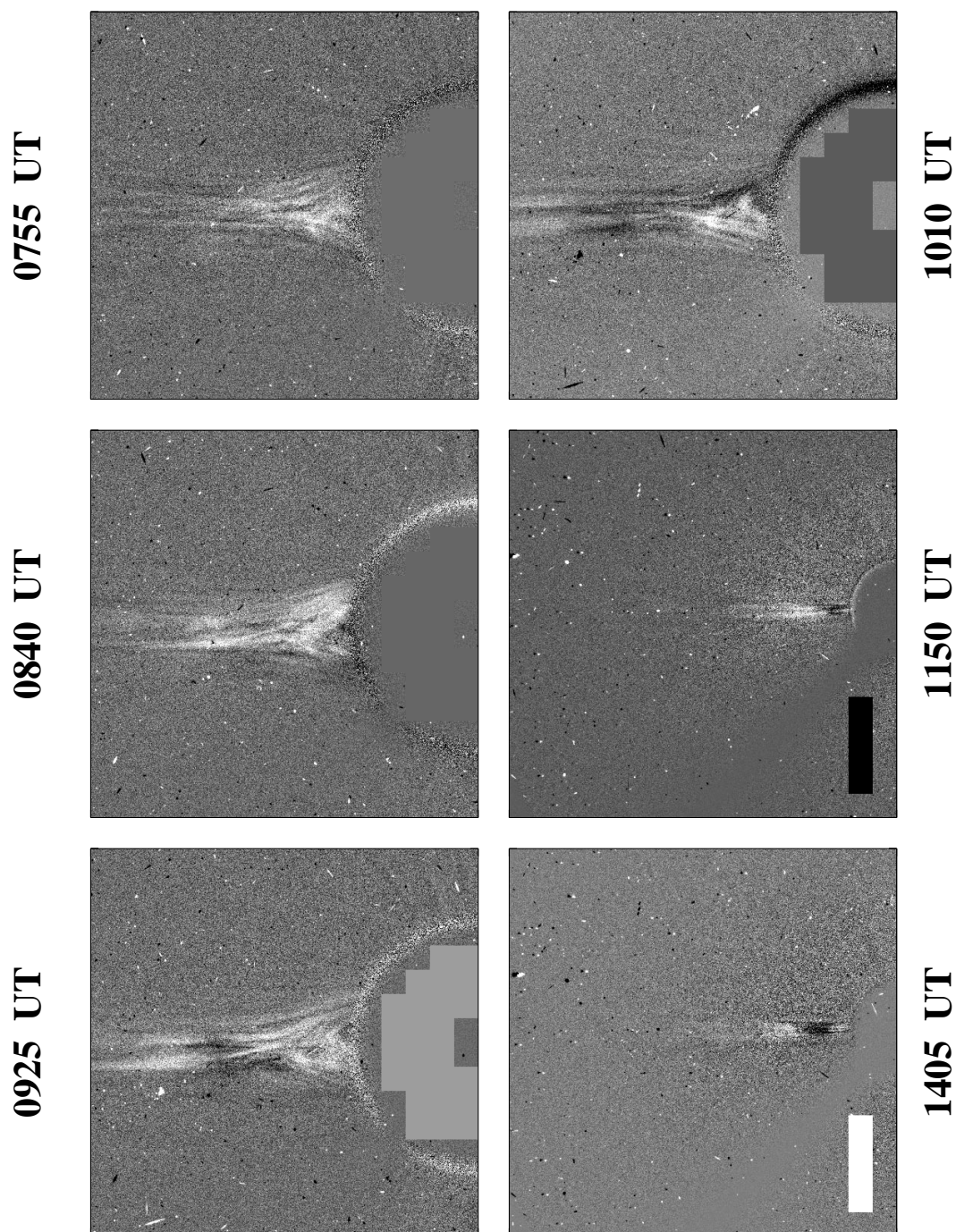SHEELEY, JR., et al. (see 484, 473)

PLATE 13

FIG. 2.—The detachment of coronal features from the tips of helmet streamers and their outward motion through the C2 (*left and top right*) and C3 (*right*) fields of view on 1996 October 30. The panels show running difference images as in Fig. 1.

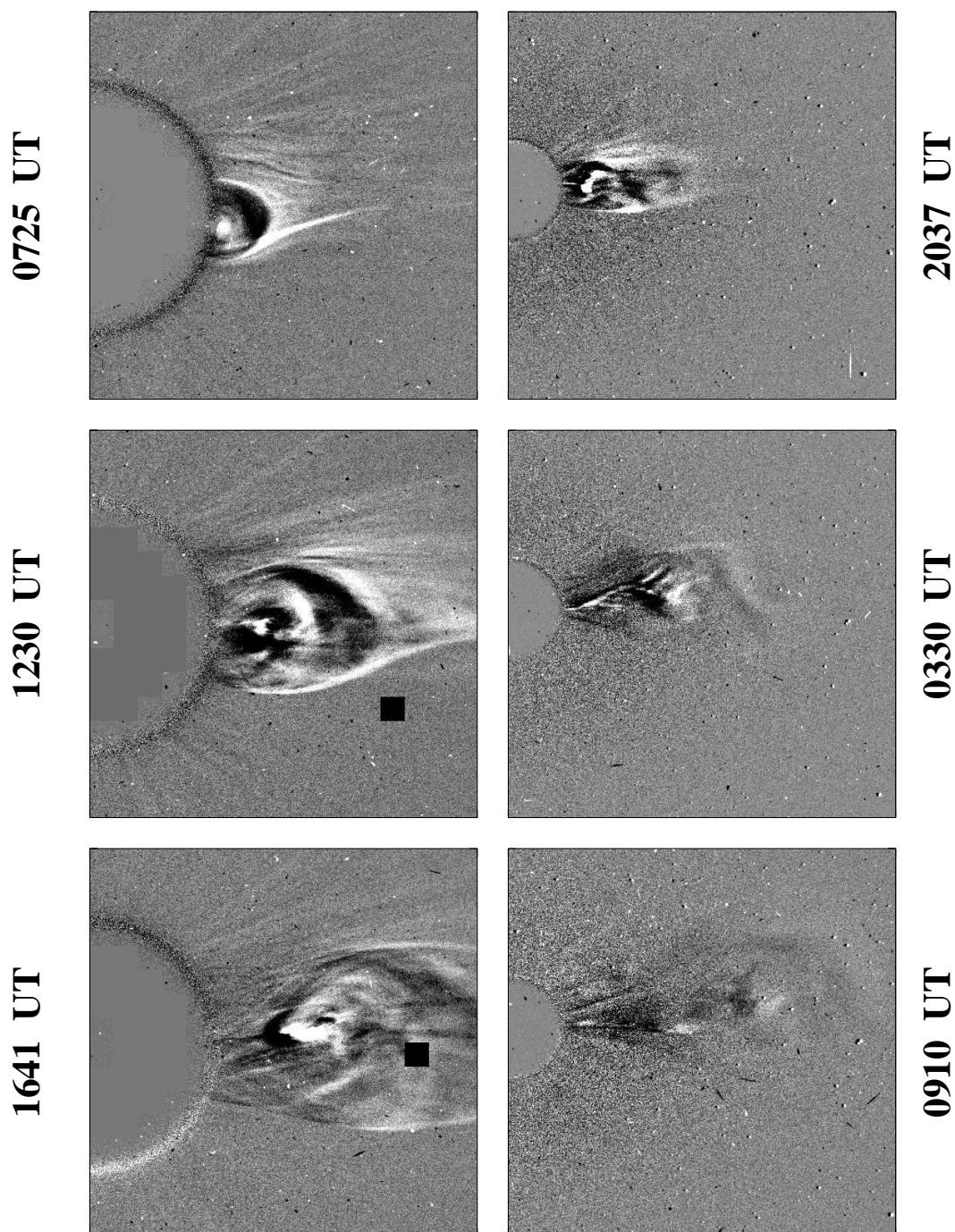SHEELEY, JR., et al. (see 484, 473)

PLATE 14

Fig. 7.—The streamer blowout mass ejection of 1996 November 5, showing the expansion and outward motion of a coronal cavity containing prominence material. The panels are running difference images as in Figs. 1 and 2.

Sheeley, Jr., et al. (see 484, 477)

PLATE 15